AIAA JOURNAL
Vol. 48, No. 4, April 2010

Technical Notes

Impact of Pressure and Temperature on the Performance of Plasma Actuators

Philippe Versailles,* Vincent Gingras-Gosselin,† and Huu Duc Vo‡
École Polytechnique de Montréal, Montréal, Québec H3T 1J4, Canada

DOI: 10.2514/1.43852

Nomenclature

F_B	=	body force induced on the fluid by the actuator per unit of actuator span, mN/m
F_{Net}	=	net actuator force of $(F_B - F_\tau)$ per unit of actuator span, mN/m
F_τ	=	shear force at the wall, induced by the plasma actuator flow, per unit of actuator span, mN/m
u	=	axial velocity component, m/s
v	=	normal velocity component, m/s
x	=	axial position with respect to actuator, m
y	=	normal position above surface, m
ρ	=	air density, kg/m^3

I. Introduction

SINGLE dielectric barrier discharges (SDBD) or plasma actuators are fluidic actuators consisting of two offset electrodes: one exposed to the air and one hidden in a dielectric material, as shown in Fig. 1. When an AC voltage of a few kilovolts at a few kilohertz is applied across the electrodes, the air over the hidden electrode is partially ionized. The charged particles subject to the electric field are accelerated and transfer their momentum to the air through collisions. The result is equivalent to a body force imparted on the flow to create a jet.

The first applications involved external flows, such as around aircraft wings [1,2] operating at atmospheric temperatures and at or below atmospheric pressures. Baughn et al. [3] and Porter et al. [4] measured SDBD actuators' forces at atmospheric conditions. Benard et al. [5] studied the effectiveness of the actuators between 0.2 and 1 atm. Flow measurements for constant actuator input voltage and frequency showed a maximum induced air velocity at 0.6 atm. Other measurements by Gregory et al. [6] showed a linear relation between the induced force and the pressure, between 0.18 and 0. 8 atm, for constant power levels.

More recently, internal flow applications of plasma actuators in gas turbine engines [7] have been proposed. These advanced concepts require operation of the actuators at high pressures and temperatures, for which very little is known about their behavior. Segawa et al. [8] tested alumina ceramic and quartz glass plasma actuators up to 600°C. Using Schlieren photography, they showed a decrease in performances of the actuators with increasing temperatures. However, the actuators were in a circular configuration, and force measurements were not made.

The objective of the present work is to provide a quantitative assessment of the behavior of SDBD actuators for pressures and temperatures higher than standard atmospheric conditions. In two experiments, the effects of pressure (100 to 690 kPa at room temperature) and temperature (30–200 $\pm$ 2°C at atmospheric pressure) on the induced force of conventional SDBD actuators are independently assessed. The experimental setups are first presented in the next section, followed by the analysis and discussion of the results in Sec. III and the main conclusions in Sec. IV.

II. Experimental Setups

A. High-Pressure Apparatus

The experimental setup (see Fig. 2) consists of a 61-cm-long transparent cast acrylic cylinder, with a 15.2 cm outside diameter and a wall thickness of 9.53 mm, sandwiched between two square $20.32 \times 20.32 \times 2.54$ cm acrylic end plates. The apparatus is designed for gauge pressures up to 690 kPa; the accuracy in pressure measurements is $\pm$6.89 kPa. The cylinder is intended to be long enough to ensure that negligible recirculation is induced inside, as verified later, such that the actuator can be considered to operate in static air. Four holes are placed in one of the end plates: one for a thermocouple to monitor the temperature inside the enclosure (which also serves as the gas inlet from the shop air supply), one for the air outlet, one for the high-voltage wire, and one for the ground wire. The plasma actuator is placed near this end plate, with the hidden electrode grounded and the exposed electrode connected to the high-voltage cable. Figure 3 shows the configuration of the plasma actuator used in this experiment. The electrodes are made of 0.076-mm-thick tinned copper foil tape (4 and 12.7 mm wide for the exposed and hidden electrodes, respectively). They are placed on either side of a 1.6-mm-thick Teflon sheet and separated axially by a 2 mm gap. To reduce the quantity of parasitic plasma that can form in the neighborhood of the grounded electrode, Kapton tape (with an approximate thickness of 0.08 mm) is placed over this electrode. A Minipuls 2 high-voltage generator from Electrofluid Systems (160 kW, 0–25 $kV_{p\text{-}p}$ and 5–30 kHz) is used to generate the sinusoidal input to the actuator.

Particle image velocimetry (PIV) measurements of the flow near the plasma actuator are made to deduce the induced body force. The PIV system from Dantec Dynamics is composed of a New Wave solo laser (neodymium-doped yttrium aluminum garnet laser, wavelength: 532 nm) and a Hi-Sense M2E eight-bit camera (1600$\times$ 1186 pixels). Light-scattering olive oil particles, on the order of 1 μm, are introduced into the enclosure via one of the end plate holes before pressurization and are illuminated by a laser sheet shone through one of these end plates (see Fig. 2). The time delay between two laser pulses is in the 50–200 ms range, depending on the maximum displacement of the fastest particle in the interrogation

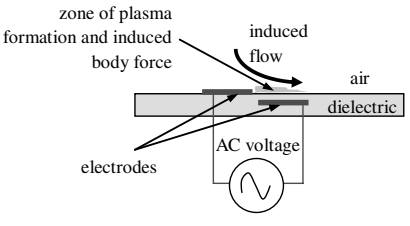

Fig. 1 SDBD (plasma) actuator.

Received 18 February 2009; accepted for publication 2 October 2009.

*Graduate Student, Department of Mechanical Engineering.
†Undergraduate Student, Department of Mechanical Engineering.
‡Assistant Professor, Department of Mechanical Engineering. Member AIAA.

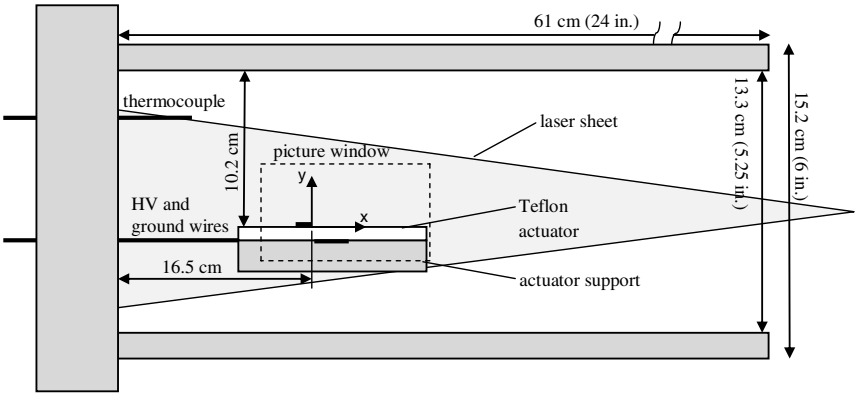

Fig. 2 High-pressure experimental apparatus. (HV denotes high voltage.)

areas of 32 × 32 pixels. Furthermore, an overlap of 50% has been used in the computation of the cross correlation in the analysis software FlowManager. To assess the effects of the tube curvature on the velocity measurements, a picture of a millimeter-meshed paper placed above the plasma actuator is taken. Then, the maximum deviation of the points in the y direction is computed using FlowManager as a few hundredths of a millimeter, confirming that the error due to tube curvature is negligible. Measurements of the velocity component in the x direction can be shown theoretically to be unaffected by the tube curvature.

B. High-Temperature Apparatus

To test plasma actuators at high temperatures, an oven able to reach 480°C is modified by machining a hole at its bottom, through which will pass an aluminum mast that holds the actuator plate and connects it to an L-shape force balance below the oven (see Fig. 4). A thermocouple is also inserted above the actuator plate to measure the air temperature. At the base of the mast, a pivot is connected to a perpendicular arm on which the end rests on an electronic scale with a 0.01 g precision. This setup allows a threefold amplification of the net actuator force.

The high-temperature plasma actuator, as shown in Figs. 4 and 5, is made up of two stainless steel electrodes (0.30 mm thick and 12.7 mm wide by 152 mm long) separated by a 5-mm-thick ceramic sheet that serves both as a dielectric and an actuator plate. There is no axial gap between the electrodes for this actuator, as it is found that this configuration gives the best performance. The electrodes are held to the ceramic with a high-temperature ceramic adhesive that is also used as a dielectric material placed over the upstream part of the grounded electrode (see Fig. 5) to prevent parasitic plasma that would otherwise form in this region. The Minipuls 2 high-voltage generator described previously is used to generate the sinusoidal input to the plasma actuator.

III. Results and Discussion

A. Plasma Actuation at High Pressure

The effect of pressure on the plasma extent is shown in Fig. 6. The room temperature is 23 ± 2°C, the voltage is 22 $kV_{p\text{-}p}$, and the frequency is 13. 5 kHz. Figure 6 shows a decrease in the plasma extent and the density with increasing pressure, with very little plasma produced at 271 kPa. Above this pressure, no plasma generation is observed visually.

Velocity profiles derived from PIV measurements are shown in Fig. 7. The related actuator configurations are summarized in Table 1.

Twenty-six PIV measurements, taken out of phase over several input cycles, are used to obtain equally spaced instantaneous flowfields in a reconstituted cycle that are then averaged to find a

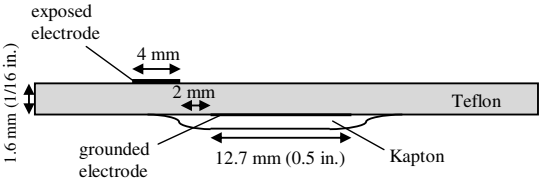

Fig. 3 SDBD actuator for high-pressure experiment.

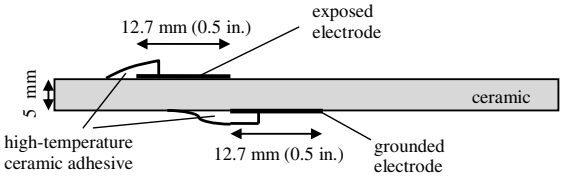

Fig. 5 High-temperature ceramic SDBD actuator.

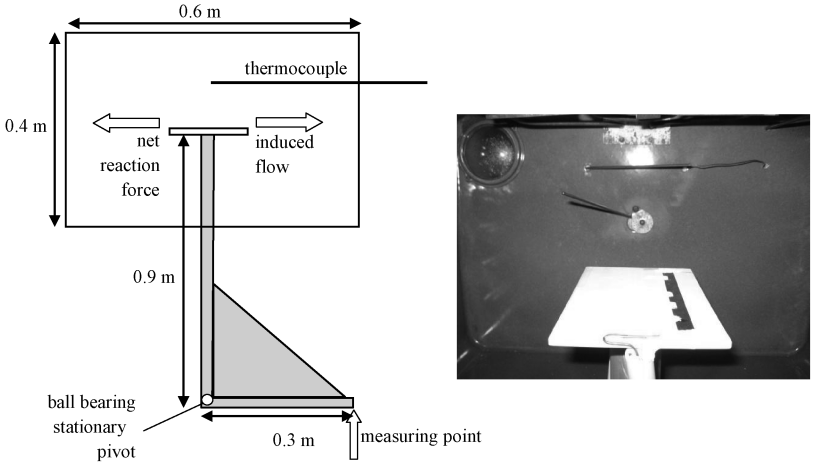

Fig. 4 High-temperature experimental apparatus.

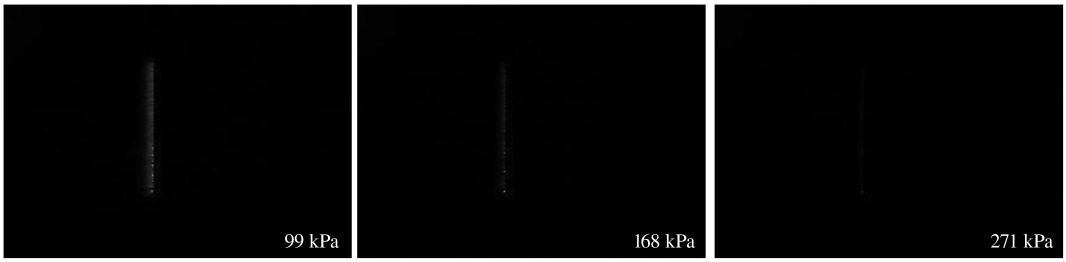

Fig. 6 Pictures of plasma at 22 kV$_{p\text{-}p}$ and 13.5 kHz for different air pressures.

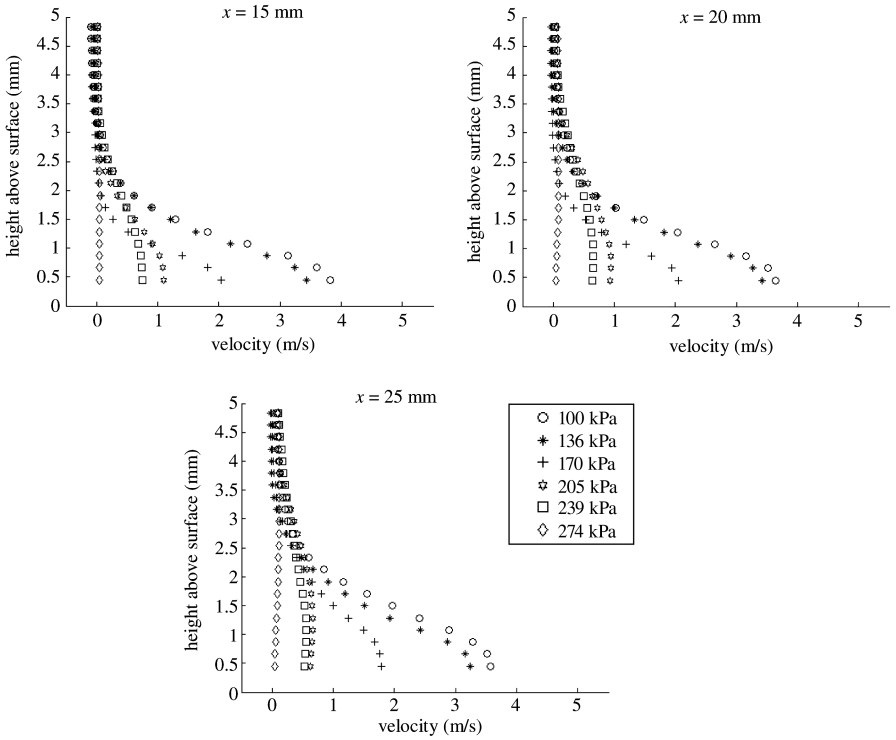

Fig. 7 Velocity profiles for input configuration 1 at $x = 15$, 20, and 25 mm for different pressures.

time-averaged velocity vector field. The axial direction is along the x axis, with $x = 0$ located at the downstream edge of the exposed electrode (see Fig. 2). The relative error of these PIV measurements falls, between 2.5 and 5% (see Prasad et al. [9] and Adrian et al. [10]). It must be noted that the velocity vectors very near the surface could not be measured due to laser reflections from the surface. All the velocity profiles tend toward 0 m/s beyond 3 mm above the surface, which means that the cylindrical enclosure is large enough to maintain the rest of the enclosed air nearly static during the operation of the actuator. Figure 7 shows the velocity profiles at $x = 15$, 20, and 25 mm for input configuration 1. Figure 8 shows similar data for input configurations 2 and 3 at $x = 25$ mm. A drop of induced velocity with increasing pressure is observed on these two figures. However, for configurations 2 and 3, by increasing both the input voltage amplitude and the applied frequency, one obtains higher induced velocities for the same pressure when compared with configuration 1.

To estimate the equivalent body force F_B imparted by the actuator on the fluid, a control volume extending from upstream to downstream of the actuator is set up, as shown in Fig. 9.

Table 1 Actuator input configurations for high-pressure tests with PIV

Input configuration	Frequency, kHz	Voltage peak to peak, kV
1	10	15
2	13.5	20
3	17	20.5

The total force of the actuator on the air can be obtained from a momentum balance on the control volume, defined in Fig. 9 (as shown in [3]). With the assumptions of incompressible flow, uniform static pressure, and negligible viscous stress on the upper surface of the control volume, the momentum balance in the x direction gives

$$F_B - \int_{l1} \mu \frac{\mathrm{d}u}{\mathrm{d}y}\,\mathrm{d}x = -\int_{l2} \rho u^2\,\mathrm{d}y + \int_{l3} \rho uv\,\mathrm{d}x + \int_{l4} \rho u^2\,\mathrm{d}y \quad (1)$$

The second term on the left-hand side represents the viscous shear force F_τ on the fluid at the wall. All along $l1$, the derivative $\mathrm{d}u/\mathrm{d}y$ is approximated from the velocity of the first PIV measurement point above the surface divided by the height of this point. Figure 10 shows the variation of F_B with pressure. These results exhibit a nonlinear decrease of induced force on the fluid with increasing pressure. This drop is most pronounced between 135 and 200 kPa, an observation that can also be deduced from the relatively large changes in the velocity profiles in Figs. 7 and 8. Moreover, the inflection points found in the pressure range 150–200 kPa and the negative second derivative of the three sets of data below these points seem to indicate the occurrence of maximum forces at subatmospheric pressures, which is consistent with the results from Benard et al. [5].

Two explanations can be proposed for the drop in F_B with increasing pressure above a certain optimum value. The first is the linear increase of threshold voltage (for plasma formation) with the pressure that, for a constant input voltage amplitude, implies a reduced proportion of the input cycle over which plasma is present.

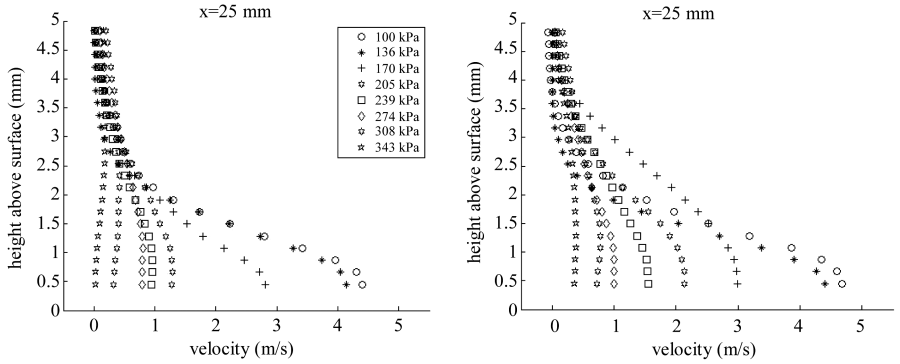

a) b)

Fig. 8 Velocity profile at $x = 25$ mm for input configurations: a) 2 (13.5 kHz and 20 kV) and b) 3 (17 kHz and 20.5 kV).

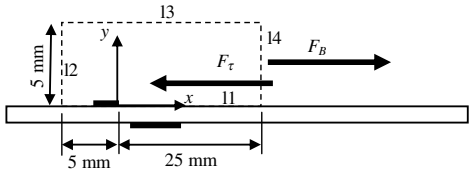

Fig. 9 Control volume for induced force computation.

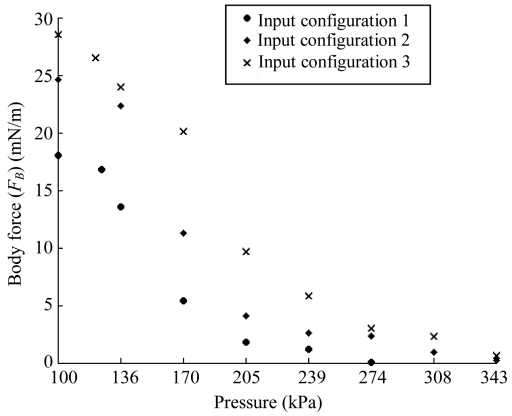

Fig. 10 Induced force F_B vs gauge pressure for input configurations 1, 2, and 3.

The second explanation, inferred from [11], is the reduction of the mean free path λ of the particles. For an increasing pressure, λ drops from the rise in density, and the charged particles have less kinetic energy when they collide. Therefore, they transfer lower momentum to the air, and it results in lower F_B.

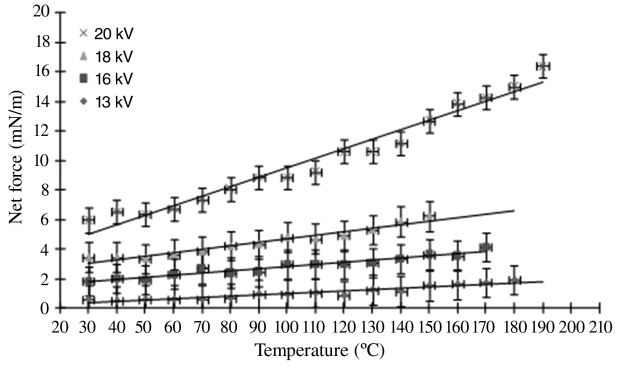

Fig. 11 Net actuator force vs air temperature for input frequency of 9.4 kHz at different voltages.

B. Plasma Actuation at High Temperature

The effect of temperature is examined next. The operating conditions are atmospheric pressure, input voltages in the 13–20 $kV_{p\text{-}p}$ range, and an actuator frequency of 9.4 kHz. Because F_{Net} is equal to the vectorial sum of two opposite forces, F_B and F_τ, it can be considered as a conservative estimate of the induced force F_B on the air by the actuator. Moreover, because the power consumption of the plasma actuator increases with the temperature, a point comes at which the high-voltage generator cannot supply the necessary power output. Hence, a temperature ceiling of 200°C is imposed on this experiment.

Figure 11 shows an almost linear increase of F_{Net} with increasing temperature. The rise in force can be significant, approximately doubling between 30 and 150°C (±2°C) for all input voltages. A possible explanation for the increase in induced force with temperature at constant pressure is the decrease in air density and, therefore, of the mean free path λ of the particles [11].

IV. Conclusions

The following conclusions can be made:

1) For a given actuator input, the plasma density and extent decrease with increasing pressure.

2) The induced velocity and body force on the fluid diminish nonlinearly with increasing pressure, exhibiting a pronounced drop between 135 and 200 kPa.

3) The induced force on the fluid increases almost linearly with increasing temperatures between 30 and 200°C.

For applications in propulsion, a benefit is that, although the effectiveness of the actuators decreases with increasing pressure, the opposite trend observed with increasing temperature may compensate for this decrease in the actuators' performances.

Acknowledgments

The authors would like to thank the Natural Sciences and Engineering Research Council of Canada, as their funding was used for most of this research. The authors also gratefully acknowledge the support of Njuki W. Mureithi and Kenny Huynh for the particle image velocimetry system; Bruno Detuncq, Anne Dionne, Jean-Marie Béland, and François Morin for their technical help; and Wajid Ali Chishty from the National Research Council for his advice.

References

[1] Corke, T., and Post, M., "Overview of Plasma Flow Control: Concepts, Optimization, and Applications," AIAA Paper 2005-563, 2005.

[2] Goeksel, B., Rechenberg, I., Greenblatt, D., and Paschereit, C. O., "Steady and Unsteady Plasma Wall Jets for Separation and Circulation Control," AIAA Paper 2006-3686, 2006.

[3] Baughn, J. W., Porter, C. O., Peterson, B. L., McLaughlin, T. E., Enloe, C. L., Font, G. I., and Baird, C., "Momentum Transfer for an Aerodynamic Plasma Actuator with an Imposed Boundary Layer," AIAA Paper 2006-168, 2006.

[4] Porter, C. O., Baughn, J. W., McLaughlin, T. E., Enloe, C. L., and Font, G. I., "Temporal Force Measurements on an Aerodynamic Plasma Actuator," AIAA Paper 2006-104, 2006.

[5] Benard, N., Balcon, N., and Moreau, E., "Electric Wind Produced by a Surface Dielectric Barrier Discharge Operating in Air at Different Pressures: Aeronautical Control Insights," *Journal of Physics D: Applied Physics*, Vol. 41, No. 4, 2008, Paper 042002. doi:10.1088/0022-3727/41/4/042002

[6] Gregory, J. W., Enloe, C. L., Font, G. I., and McLaughlin, T. E., "Force Production Mechanisms of a Dielectric-Barrier Discharge Plasma Actuator," AIAA Paper 2007-185, 2007.

[7] Vo, H. D., "Rotating Stall Suppression in Axial Compressors with Casing Plasma Actuation," AIAA Paper 2007-3845, 2007.

[8] Segawa, T., Furutani, H., and Yoshida, H., "Wall Normal Jet Under Elevated Temperatures Produced by Surface Plasma Actuator," AIAA Paper 2007-784, 2007.

[9] Prasad, A. K., Adrian, R. J., Landreth, C. C., and Offutt, P. W., "Effect of Resolution on the Speed and Accuracy of Particle Image Velocimetry Interrogation," *Experiments in Fluids*, Vol. 13, Nos. 2–3, 1992, pp. 105–116. doi:10.1007/BF00218156

[10] Adrian, R. J., Meinhart, C. D., and Tomkins, C. D., "Vortex Organization in the Outer Region of the Turbulent Boundary Layer," *Journal of Fluid Mechanics*, Vol. 422, Nov. 2000, pp. 1–54. doi:10.1017/S0022112000001580

[11] Sarra-Bournet, C., "Design et Réalisation d'un Réacteur Plasma à Pression Atmosphérique pour des Traitements de Surfaces dans le Domaine des Biomatériaux," Master's Thesis, Univ. Laval, Québec City, Québec, Canada, 2007.

N. Chokani
Associate Editor